

# MODELING OF BREAKUP EVENTS IN MEDIUM EARTH ORBIT

M. M. Pellegrino<sup>(1)</sup>, D. J. Scheeres<sup>(1)</sup>, and B. J. Streetman<sup>(2)</sup>

<sup>(1)</sup>University of Colorado Boulder, 3775 Discovery Drive, 429 UCB-CCAR, Boulder, CO, USA Email: {marielle.pellegrino, scheeres}@colorado.edu

<sup>(2)</sup>Charles Stark Draper Laboratory, Inc., 555 Technology Square, Cambridge, MA, USA, Email: bstreetman@draper.com

## ABSTRACT

This paper investigates how breakup events evolve in Medium Earth Orbit. It considers how the known instabilities in the orbital regime will influence the long term dynamics from these fragment clouds. Two cases are studied, a collision and an explosion, in three constellations, Galileo, GPS, and GLONASS. This paper explores the eccentricity growth and reentry of the objects in the fragment cloud as well as how the resonance structure aligns with the reentry of certain fragments.

Keywords: MEO, breakup, GNSS, collision, explosion.

## 1. INTRODUCTION

Medium Earth orbit (MEO), home to the world's global navigation satellite systems (GNSS), is affected by chaotic behavior due to luni-solar resonances. This chaos is caused by the gravitational pulls of the Sun and Moon which cause the eccentricity of these orbits to increase rapidly, on the order of decades to centuries. Previous work has studied the long term behavior of satellites in this regime in determining possible stable regions for graveyard orbits or utilizing the unstable regions for reentry trajectories, essentially using a "free" ride back to Earth [8, 2, 5]. These studies have all focused on satellites in the region which are have very low area-to-mass ratios. There have been a few studies of, high area-to-mass, HAMR objects in a nominal GPS orbit, but not nearly as extensive of a survey of the varying neighboring orbits [1, 6]. Because orbital debris often take on the form of high area-to-mass ratio (HAMR) objects, it is important though when studying the health of possible orbital regimes to also include studies of high area-to-mass ratio objects.

From previous work we know that the region's chaotic maps changed with varying area-to-mass ratios [6]. Some regions that were determined to be stable using low area-to-mass ratios became highly unstable for higher area-to-mass ratios. Likewise, previously unstable regions appeared stable with higher area-to-mass ratios. This work

further validated the need to incorporate debris studies of HAMR objects in the region. In addition, recent work on characterizing the performance of doubly averaged dynamics allows us to confidently use doubly averaged tools in order to conduct surveys of the region with computational efficiency [7].

These recent studies not only provide the motivation for studying varying area-to-mass ratio objects but also the tools to do so. This paper will focus on understanding the long term behavior of two breakup events in MEO. The first breakup event is what Johnson et al. characterize as a low intensity explosion, represents an event like a battery exploding on a satellite in this orbital regime [3]. The second event we will characterize is a high intensity explosion, representing an event like a collision between two satellites. By analyzing both types of events, we will be able to understand how debris from breakup events will interact with the luni-solar resonances in this orbital regime. This analysis will be crucial in determining whether a potential graveyard orbit could be a viable solution for medium Earth orbit or after dynamic events in the region the debris can interact with nearby unstable regions and be a potential hazard to functioning spacecraft in nearby orbits.

## 2. DYNAMICAL MODEL

The dynamical model incorporates three perturbations: the effects due to the oblateness of the Earth, the third body effects due to the Sun and Moon, and the effects due to solar radiation pressure (SRP). For computational efficiency, the averaged formulations of these perturbations are used. The dynamics due to the Earth's oblateness is singly averaged; its effects are averaged over the orbital period of the piece of debris. The third body effects are doubly averaged; they are averaged once over the piece of debris's orbit and a second time over the perturbing bodies orbit. The final perturbation, SRP, is either singly or doubly averaged. This choice depends on the area-to-mass ratio of the debris fragment. An area-to-mass ratio larger than  $1 \text{ m}^2/\text{kg}$  requires a singly averaged model because the large magnitude changes in eccentricity are missed by the doubly averaged model. For ob-

jects with lower area-to-mass ratios, the doubly averaged model suffices and runs much faster [7].

## 2.1. Milankovitch Elements

The forms of the averaged solutions will be in terms of the scaled Milankovitch elements which are defined as

$$\mathbf{e} = \frac{1}{\mu} \tilde{\mathbf{v}} \cdot \mathbf{H} - \hat{\mathbf{r}} \quad (1)$$

$$\mathbf{h} = \frac{\tilde{\mathbf{r}} \cdot \mathbf{v}}{\sqrt{\mu a}} \quad (2)$$

This expressions uses dyadic notation which denotes the cross product in the form of a dyad [9]:

$$\tilde{a} = a_x(\hat{\mathbf{z}}\hat{\mathbf{y}} - \hat{\mathbf{y}}\hat{\mathbf{z}}) + a_y(\hat{\mathbf{x}}\hat{\mathbf{z}} - \hat{\mathbf{z}}\hat{\mathbf{x}}) + a_z(\hat{\mathbf{y}}\hat{\mathbf{x}} - \hat{\mathbf{x}}\hat{\mathbf{y}}) \quad (3)$$

The eccentricity vector is  $\mathbf{e}$  and  $\mathbf{h}$  is the scaled angular momentum vector. Since we are focused on gravitational and SRP perturbations formulated as conservative forces, the semi-major axis will be constant on average in general, thus validating our use of the scaled Milankovitch elements. The velocity vector is denoted by  $\mathbf{v}$ , angular momentum by  $\mathbf{H}$ , position vector by  $\mathbf{r}$ , and semi-major axis by  $a$ . Together these vectors define eccentricity, inclination, argument of periapsis, and longitude of the ascending node. The scaled Milankovitch elements also exhibit two constraints  $\mathbf{e} \cdot \mathbf{h} = 0$  and  $\mathbf{e} \cdot \mathbf{e} + \mathbf{h} \cdot \mathbf{h} = 1$ .

## 2.2. Earth's Oblateness

The oblateness of the Earth is characterized in terms of singly-averaged dynamics as Equations 4 and 5

$$\dot{\mathbf{h}}_{20} = -\frac{3nC_{20}}{2a^2h^5} (\hat{\mathbf{p}} \cdot \mathbf{h}) \tilde{\mathbf{p}} \cdot \mathbf{h} \quad (4)$$

$$\dot{\mathbf{e}}_{20} = -\frac{3nC_{20}}{4a^2h^5} \left( \left( 1 - \frac{5}{h^2} (\hat{\mathbf{p}} \cdot \mathbf{h})^2 \right) \tilde{\mathbf{h}} + 2(\hat{\mathbf{p}} \cdot \mathbf{h}) \tilde{\mathbf{p}} \right) \cdot \mathbf{e} \quad (5)$$

where  $C_{20}$  is the second degree zonal gravitational coefficient. The polar axis of the Earth is represented by  $\hat{\mathbf{p}}$ .

## 2.3. Third Body Gravitation

The doubly-averaged third body gravitational perturbations in terms of the Milankovitch elements are Equations 6 and 7.

$$\dot{\mathbf{h}} = -\frac{3\mu_p}{4na_p^3h_p^3} \hat{\mathbf{H}}_p \cdot (5\mathbf{e}\mathbf{e} - \mathbf{h}\mathbf{h}) \cdot \tilde{\mathbf{H}}_p \quad (6)$$

$$\dot{\mathbf{e}} = -\frac{3\mu_p}{4na_p^3h_p^3} (\hat{\mathbf{H}}_p \cdot (5\mathbf{e}\mathbf{h} - \mathbf{h}\mathbf{e}) \cdot \tilde{\mathbf{H}}_p - 2\tilde{\mathbf{h}} \cdot \mathbf{e}) \quad (7)$$

where  $a_p$  is the semi-major axis of the perturbing body,  $h_p$  is the scaled angular momentum of the perturbing body, and  $\hat{\mathbf{H}}_p$  is the unit vector of the angular momentum of the perturbing body.

## 2.4. Solar Radiation Pressure

For high-area-to-mass ratio (HAMR) objects,  $\geq 1\text{m}^2/\text{kg}$ , we use the singly averaged model, Equations 8 and 9.

$$\dot{\mathbf{h}}_{srp} = -\frac{3}{2} \sqrt{\frac{a}{\mu}} \frac{P_0 \eta (1 + \rho)}{d^2} \tilde{\mathbf{d}}_s \cdot \mathbf{e} \quad (8)$$

$$\dot{\mathbf{e}}_{srp} = -\frac{3}{2} \sqrt{\frac{a}{\mu}} \frac{P_0 (1 + \rho) \eta}{d^2} \tilde{\mathbf{d}}_s \cdot \mathbf{h} \quad (9)$$

The distance between the Sun and the satellite (or more roughly the Earth) is  $d_s$ , and  $\tilde{\mathbf{d}}_s$  is the unit vector from Sun to Earth.

The other variables relate to the satellite's properties. The ratio of reflectivity,  $\rho$ , describes one of the material properties of the surface of the satellite, specifically how the Sun's light is reflected and varies between 0 and 1. Because this is not a known parameter output by the breakup cloud, we assume the strongest value of 1. The area-to-mass ratio,  $\eta$ , also affects how strongly the satellite is influenced by SRP and is computed as  $\eta = \frac{area}{mass} \text{m}^2/\text{kg}$ .

The doubly averaged formulation, used for all fragments  $< 1\text{m}^2/\text{kg}$ , is modeled in Equations 10 and 11.

$$\dot{\mathbf{h}}_{srp} = -\frac{2\pi(1 - \cos \Lambda)}{T_s \cos \Lambda} \tilde{\mathbf{H}}_s \cdot \mathbf{h} \quad (10)$$

$$\dot{\mathbf{e}}_{srp} = -\frac{2\pi(1 - \cos \Lambda)}{T_s \cos \Lambda} \tilde{\mathbf{H}}_s \cdot \mathbf{e} \quad (11)$$

where the SRP parameter is defined as

Table 1: Initial Conditions for Breakup events.

GNSS	a (km)	e	i (deg)	$\omega$ (rad)	$\Omega$ (rad)	$\nu$ (rad)
GPS	26559	0.003	55°	5	6	$2\pi - 5$
Galileo	29600	0.003	56°	5	6	$2\pi - 5$
GLONASS	25400	0.003	64.8°	5	6	$2\pi - 5$

$$\tan \Lambda = \frac{3(1 + \rho)P_0\eta}{2V_{lc}H_s} \quad (12)$$

where  $V_{lc}$  is the local circular speed of the orbiter,  $H_s$  is the norm of the Sun's angular momentum, and  $T_s$  is the Earth's orbital period about the Sun.

### 3. FRAGMENT CLOUD

NASA's Orbital Debris Program office provided the breakup fragment clouds for each of the events discussed in this paper from their breakup model [3]. The first event discussed is a low intensity event. This would be representative of an explosion or other type of break event. This event is low energy and results in a small cloud of fragments about the initial conditions of the original satellite. The other event modeled is of a collision, because the nominal orbits of these objects are in a circular orbit, we modeled the collision event to be where the two satellites had a difference of right ascension of the ascending node (RAAN) of  $\pi$  and collided at the equator. Because all the constellations are heavily inclined the collision is catastrophic, a relative magnitude between the two objects close to 6 or 7 km/s. This event results in a larger swath of fragments, some which are no longer bound to Earth orbit and some which reenter immediately.

Table 1 shows the initial conditions for the events in terms of the orbital elements, semi-major axis (a), eccentricity (e), inclination (i), argument of perigee ( $\omega$ ), RAAN ( $\Omega$ ),

and true anomaly ( $\nu$ ). For simplicity, each type of event (breakup and collision) use the same initial conditions.

The impactor's initial conditions for the collision event is the same as the parent object described in Table 1 but is out of phase by  $\pi$  in RAAN and true anomaly.

## 4. GALILEO

In this section, we will detail how to fragment clouds evolve with long term simulations in the Galileo constellation. The simulations were run for 200 years after each event. The mass of the satellite is representative of a Galileo FOC satellite [11].

### 4.1. Breakup

The first event represents the low-intensity breakup. This produces a fragment cloud of 378,577 fragments. The fragments themselves are binned according to size with bin numbers of 1, 10, and 100; the smaller fragments resulting in the larger binning groups.

Figure 1 shows the maximum eccentricity achieved over the 200-year simulation relative to the object's area-to-mass ratio. The three scatter plots are scaled differently depending on three characteristics of the bin: number of objects, area of the object(s), and mass of the object(s) in the bin.

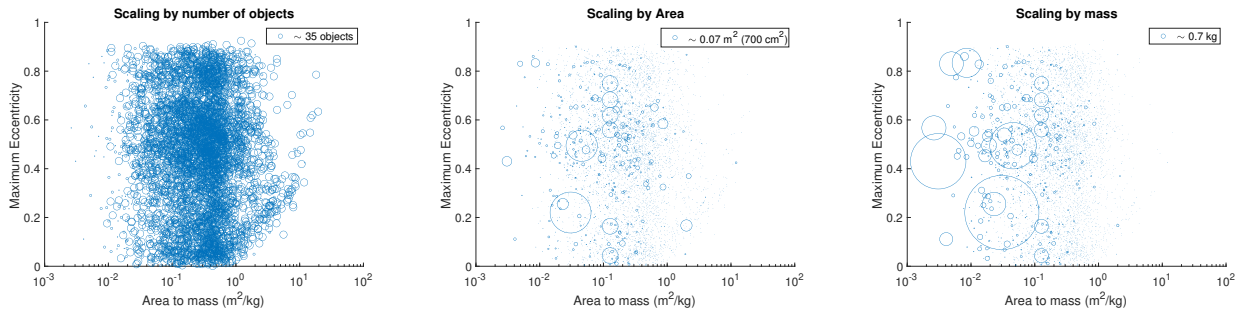


Figure 1: Maximum eccentricity of objects produced in a Galileo low-intensity breakup event

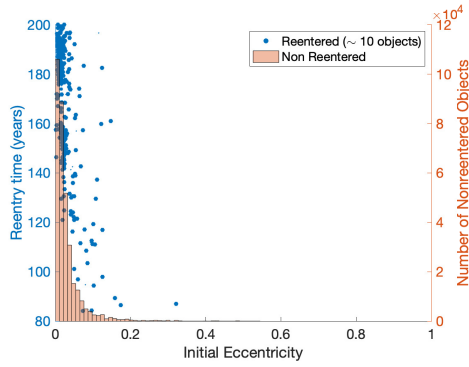


Figure 3: Reentry time of objects from the fragment cloud compared to a histogram of the number of non-reentered objects.

It is not just high-area to mass ratio objects moving toward high eccentricities. Some more massive objects start to inhabit the area.

Many objects reach a maximum eccentricity to reenter the Earth's atmosphere,  $\sim 0.78$  depending on the exact semi-major axis of the object. Figure 3 shows the reentry times for the objects that achieve the threshold of a radius of periapsis less than 122 km (where the atmosphere can begin to cause heating [4]).

Before the end of the simulation (200 years), approximately 40,000 objects reentered the Earth's atmosphere. That is about 10% of the total objects produced by the breakup event. These objects did not reenter immediately following the breakup event. They instead start to reenter close to 80 years after the breakup occurred. Most of the objects reentered are on an initially circular orbit despite the distribution extending up to 0.2 eccentricity that can be noticeably observed in Figure 3.

The final set of graphs correlates to the initial conditions of the fragments and their long term behavior. Because stability of the region is described in eccentricity, inclination, and semi-major axis, the fragments were also studied in terms of how their initial conditions compared to whether or not the object reentered. The maps indicate

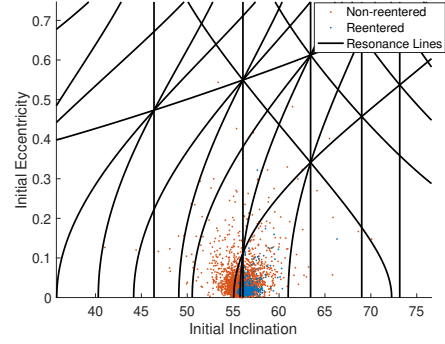


Figure 4: Initial eccentricity by initial inclination

regions of stability where resonances or lines cross [8].

For simplicity, we will examine the initial conditions in terms of initial eccentricity and inclination where the resonances are drawn for the semi-major axis for Galileo. For completeness, we also binned to specific values of semi-major axis but saw no noticeable difference in the final results and did not include those graphs.

Figures 4 and 5 show how close the resonance lines are to the debris cloud. A crossing resonance group is within the extrema of the cloud. With the truncated Figure 5 it is noticeably lurking above the bulk of the resonance cloud. However, we don't see a particularly large correlation to the resonances line crossing, the region of expected instability, and the reentered objects.

## 4.2. Collision

A higher energy event is when two satellites collide. These satellites are representative of the satellites in the regime and, as so, are massive. The impactor and parent object are modeled to be the same type of satellite. The collision is not head on; it is consistent with two satellites in near circular orbits with a RAAN separation of  $\pi(180^\circ)$  which results in  $\sim 112^\circ$  collision due to the inclination of the orbits.

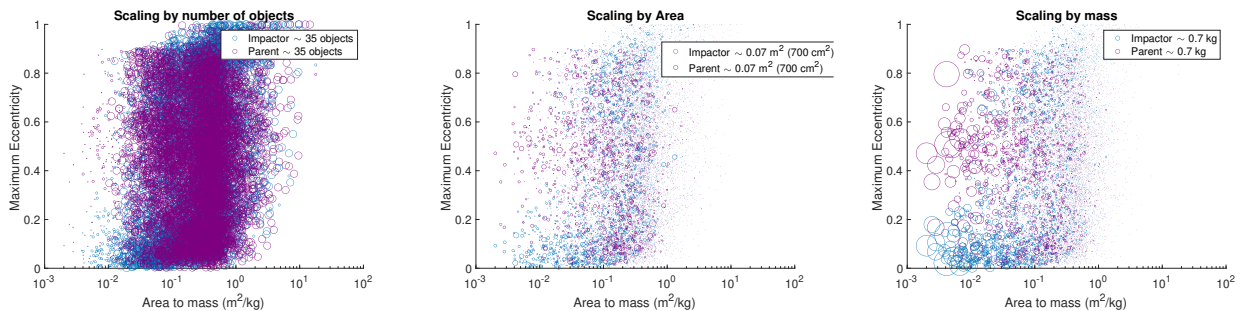


Figure 2: Maximum eccentricity of objects produced in a collision of Galileo FOC satellites

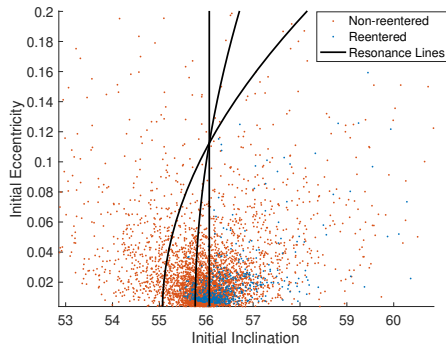


Figure 5: Truncated initial eccentricity by initial inclination

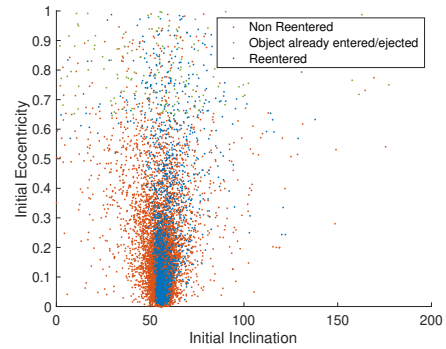


Figure 7: Initial eccentricity by initial inclination

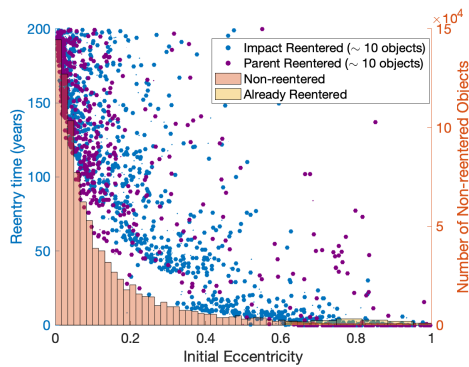


Figure 6: Reentry time of objects from the fragment cloud compared to a histogram of the number of non-reentered objects and already entered.

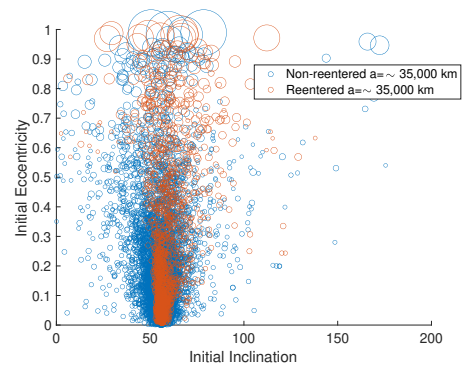


Figure 8: Initial eccentricity by initial inclination (scaled by initial semi-major axis)

The data from the breakup cloud is similar to the previous session. The modeled collision produces a fragment cloud of 1,115,000 pieces of debris, the impactor producing 511,000 pieces and the parent producing 641,000 pieces. Approximately 55,000 pieces altogether reenter or are ejected immediately following the collision leaving the rest to be studied by the long term integrations. Figure 2 shows the maximum eccentricity each group of fragments achieve after a 200 year simulation.

Because the collision case is more catastrophic and results in more pieces of debris, there are fewer large debris pieces as seen in the middle graphs (scaled by area) of Figures 1 and 2. There are some massive objects ( $\geq 1$  kg) that achieve high eccentricities particularly for the parent satellite.

Figure 6 shows the reentry times (within the 200-year simulation) for the fragment objects that do not reenter immediately following the collision, meaning that their initial conditions had a radius of periapsis above the 122 km threshold. Like the previous plots, these results are with a backdrop of the histogram of the non-reentered objects. In this case, there is also a histogram of objects that had already reentered or were ejected.

Because the collision case produces more objects with

higher initial eccentricities the reentry times reach as low a time as within the first year of the event. The bulk of the objects with more circular orbits don't reenter until after 50 years.

For the collision event, the initial eccentricity distribution varies a lot more and so does the inclination, but the bulk of the fragments are still within a few degrees of the inclination of the parent's (and impactor's) orbit.

Figure 7 shows that the bulk of the reentering objects are close to the initial inclination with slightly more reentering at higher inclinations (rather than lower inclinations) of the distribution.

Because this event results in larger changes in energy, there are some major outliers in terms of semi-major axis of the fragment cloud. Figure 8 shows that those major outliers are for higher eccentricities and the bulk of the cloud

Figure 9 shows how the resonance lines do not necessarily correlate to the reentry conditions of the fragment cloud. This stresses the need for numerical studies like this one to understand the stability of the region.

Figure 10 shows the same distribution in terms of initial eccentricity and inclination but separates the distribution based on which object produced the fragment and parent. The interesting features of this figure is that the parent ob-

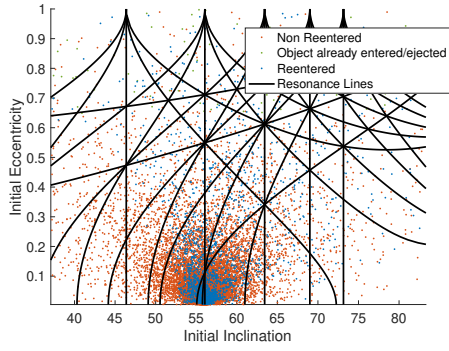


Figure 9: Initial eccentricity by initial inclination with resonance lines.

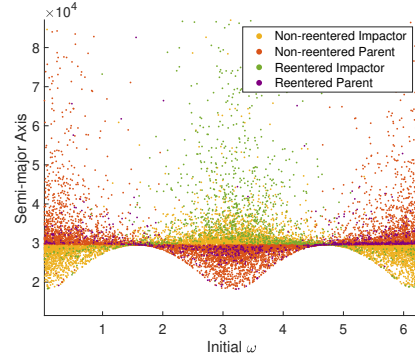


Figure 11: Initial argument of perigee and semi-major axis

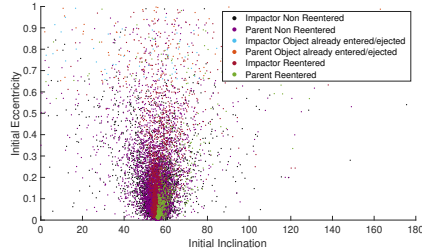


Figure 10: Initial eccentricity by initial inclination where distributions are separated by parent and impactor

ject's distribution favors reentries of higher inclinations whereas the impactors distribution of reentries does not. The impactors distribution of reentries follows the overall fragment distribution.

The main distinction from the two initial distributions are from the direction of the orbits or the argument of perigee vectors. They are flipped in that a fragment in one distributions argument of perigee will likely be the apogee in the other distribution, Figure 11. The stability of the region is known to be symmetric with a argument of perigee, in that a difference in  $\pi$  should not necessarily result in large distinctions in the behavior of the satellite, [7]. This leads to open questions about the stability of the

region and the reasons the parent and impactor's distributions result in differing reentries.

## 5. GNSS COMPARISON

In the following section we explore two additional constellations besides Galileo: GPS and GLONASS. We will compare the behavior of the fragment cloud distributions to each other. All the initial conditions can be found in Table 1.

Table 2 shows the properties of each of the different fragment clouds. GPS's collision case results in the largest number of fragments produced. All three of the explosions produced the same number of fragments. These figures and the number of objects already reentered were generated by the breakup model and not a part of this research but this helps give context to the long term behavior seen in our study. Number of objects reentered and maximum eccentricity are also included in this table but we will provide figures for more detailed analysis.

Figure 12 and 13 show the maximum eccentricity distributions for the explosion fragment clouds after the 200-year simulation. Figure 12 is a violin plot; violin plots

Table 2: Breakup Fragment Evolution

Collision Type	GPS Explosion	GPS Collision	Galileo Explosion	Galileo Collision	GLONASS Explosion	GLONASS Collision
Number of Objects in Cloud	378,577	1,202,690	378,577	1,152,871	378,577	881,082
Number of Already Reentered or Ejected Objects (% of Distribution)	-	47,214 (3.9%)	-	53,934 (4.7%)	-	31,905 (3.6%)
Number of Reentered Objects (% of Distribution)	4,387 (1.2%)	140,617 (11.7%)	40,178 (10.6%)	209,294 (18.2%)	910 (0.2%)	97,040 (11.0%)
Mean of the Maximum Eccentricity	0.093	0.296	0.457	0.455	0.421	0.378

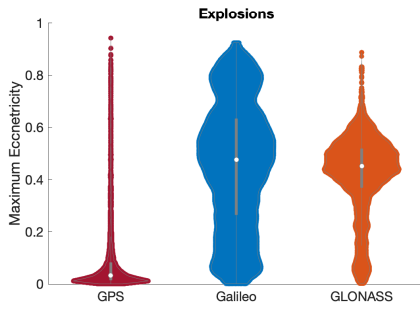


Figure 12: Violin Plots of Maximum Eccentricity for Explosions

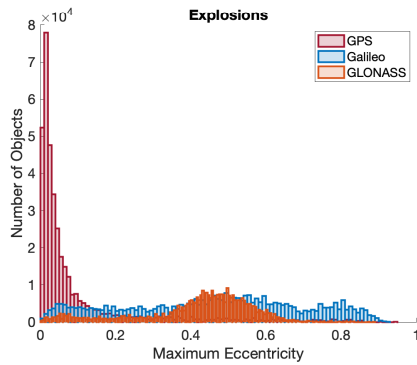


Figure 13: Histograms of Maximum Eccentricity for Explosions

are akin to histograms smoothed on their side where the largest distribution of the set is the widest part of the plot. They provide good insight on the overall distribution of the fragments but unlike histograms their widths do not necessarily correlate to an exact number of fragments. This is why Figure 13 is used to provide additional insight.

The GPS fragment cloud appears to stay near the nominal circular orbit throughout the 200-years, most of the objects not achieving an eccentricity larger than 0.1. GLONASS appears to have objects growing in eccentricity to about 0.5 but not quite achieving the very high eccentricities that results in reentries. Galileo's distribution in comparison is more uniform.

All three constellations achieve maximum eccentricities that result in reentries ( $e \geq \sim 0.75$  depending on the constellation). Figures 14 and 15 show the distributions of reentry times with the sets. Galileo has the largest number of fragments reentering in the simulation. GLONASS only has a few parts of the fragment cloud that reenter but some reenter in less than fifty years unlike the other sets. GPS does not have a large number of reentering objects and most reenter after 100 years.

Figure 16 and 17 show the maximum eccentricities for fragments after a collision event. Again, GPS has the most objects near its nominal orbit. The collision event does provide a larger distribution of objects that reach

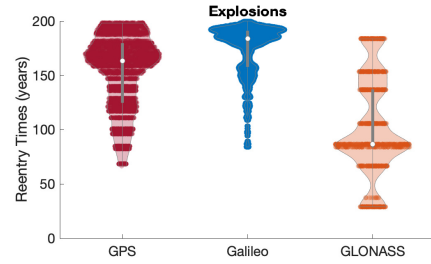


Figure 14: Violin Plots of Reentry Times for Explosion Events

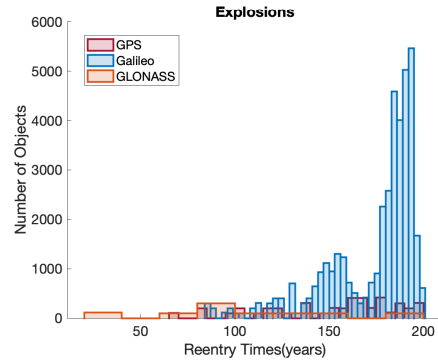


Figure 15: Histogram of Reentry Times for Collision Explosions

higher eccentricities in general. For the GLONASS case we still see the bump or large number of solutions settling near the 0.5 eccentricity. The Galileo case is still the most uniformly distributed case.

All of the constellations have maximum eccentricities that achieve reentry. Figure 18 and 19 show that majority of the reentries occur shortly after the event if they have not already entered within a few orbits of the event. Galileo has the most objects reentering after those first few years with the most entering toward the end of the 200 year simulation. Both GPS and GLONASS both have objects that reenter in later years of the simulation but a much smaller fraction of the initial few years.

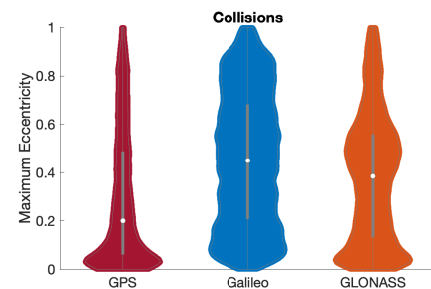


Figure 16: Violin Plots of Maximum Eccentricity for Collisions

## 6. CONCLUSION

The evolution of collision and explosion fragment clouds in MEO shows some interesting dynamics. Massive objects with relative low area-to-mass ratios resulted in reentries in the fragment cloud. A large number of those reentries occur toward the end of the 200-year simulation for the explosion case and with the collision case most of the objects reenter within a few years of the event. Even though the parent cloud and impactor differ  $\omega_p = \omega_i + \pi$  and the resonance structure is symmetric with respect to  $\omega = \omega + \pi$ , the fragment clouds of the parent and impactor behave differently. This provides motivation for some future work on how the resonances interact with the fragment cloud.

The six breakup clouds show varying behavior in the unstable environment of MEO. For explosions, Galileo and GLONASS fragment clouds wandered to higher eccentricities. However, the Galileo fragment cloud was high eccentricity enough to achieve a large number of reentries. For the collisions, the Galileo fragment cloud still showed the largest wandering to higher eccentricities but most of the fragments reentered within the decade of the event.

## ACKNOWLEDGMENTS

We would like to thank John Opiela (Jacobs JETS Contract) and NASA's Orbital Debris Program Office for providing the breakup fragment clouds used in this research.

## APPENDIX

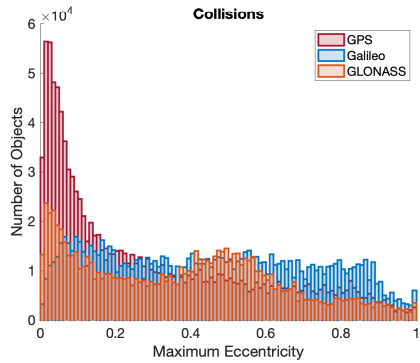


Figure 17: Maximum Eccentricity for Collision Events

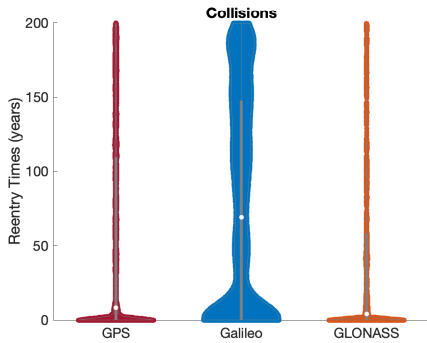


Figure 18: Violin Plots of Reentry Time for Collisions

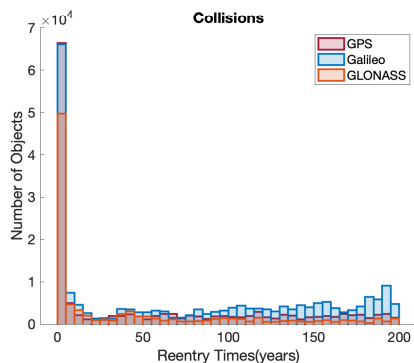


Figure 19: Maximum Eccentricity for Collision Events



Figure 20: Maximum Eccentricity for Collision Events

## REFERENCES

1. Anselmo L., Pardini C., (2009). Dynamical evolution of high area-to-mass ratio debris released into GPS orbits, *Advances in Space Research*, **43**(10), 1491–1508

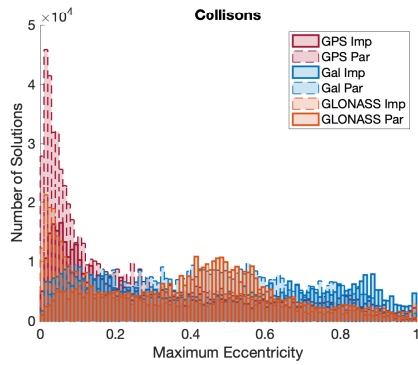


Figure 21: Maximum Eccentricity for Collision Events

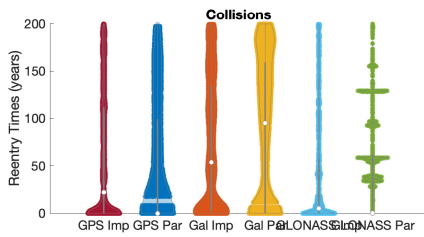


Figure 22: Reentry Times for Collision Events

2. Armellin R., San-Juan J.F., (2018). Optimal Earth's reentry disposal of the Galileo constellation, *Advances in Space Research*, **61**.4, 1097–1120
3. Johnson N. L., Krisko P.H., Liou J-C., Anz-Meador, P.D., (2001). NASA's new breakup model of EVOLVE 4.0, *Advances in Space Research*, **28**(9), 1377–1384
4. Ostrom C.L., Abercromby, K., (2017). Open Source Toolkit for Reentry Object Modeling, *AIAA Atmospheric Flight Mechanics Conference*, 4208
5. Pellegrino M.M., Scheeres D.J., (2018). Targeting Regions of Chaos In the GNSS Regime, *2018 Space Flight Mechanics Meeting*
6. Pellegrino M.M., Scheeres D.J., Streetman B.J., (2019). Long Term Dynamics of Debris Objects in MEO, *First International Orbital Debris Conference*
7. Pellegrino M.M., Scheeres D.J., Streetman B.J., (2019). Rapid Computation of MEO Satellite Deorbit Times Using Doubly Averaged Dynamics, *70th International Astronautical Congress (IAC)*
8. Rosengren A.J., Daquin, J., Tsiganis K., Alessi, E.M., Rossi, A., Valsecchi, G.B., (2016). Galileo disposal strategy: stability, chaos and predictability, *Monthly Notices of the Royal Astronomical Society*, **464**(4), 4063–4076
9. Scheeres, D.J., (2012). *Orbital Motion In Strongly Perturbed Environments*, pp. 19. Springer, New York
10. Smith A., Jones B., (1996). The new discovery, *Other Journal*, **223**(1), 1029–1101
11. Steigenberger P., Thielert S., Montenbruck O., (2018). GNSS satellite transmit power and its impact on orbit determination, *Journal of Geodesy*, **92**(6), 609–624

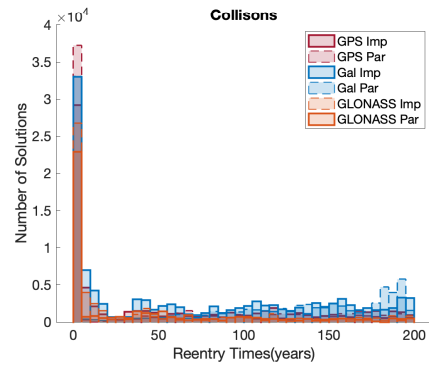


Figure 23: Reentry Times for Collision Events